In Situ Annealing Effect on Thermally Co-Evaporated $CsPbI_2Br$ Thin Films Studied via Spectroscopic Ellipsometry

Athina Papadopoulou[1,2]*, Rafikul Ali Saha[3], Maria Isabel Pintor-Monroy[1], Wenya Song[1], Itai Lieberman[1], Eduardo Solano[4], Maarten B. J. Roeffaers[3], Robert Gehlhaar[1], and Jan Genoe[1,2]*

[1]imec, Kapeldreef 75, 3001 Leuven, Belgium
[2]Department of Electrical Engineering (ESAT), KU Leuven, Kasteelpark Arenberg 10, 3001 Leuven, Belgium
[3]cMAS, Department of Microbial and Molecular Systems, KU Leuven, Celestijnenlaan 200F, 3001 Leuven, Belgium
[4]NCD-SWEET Beamline, ALBA Synchrotron Light Source, Cerdanyola del Vallès, Barcelona 08290, Spain

Keywords: Perovskite, Inorganic, Thermal Evaporation, Ellipsometry, GIWAXS, In-situ, Roughness, Phase Transitions

1. Abstract

All-inorganic cesium lead halide perovskites possess excellent thermal stability, a feature that renders them highly favorable for optoelectronic applications with elevated thermal budget. Employing a co-evaporation approach for their deposition holds promise for manufacturing at an industrial level, owing to improvements in device scalability and reproducibility. For unlocking the full potential of vacuum-evaporated perovskite thin films it is crucial to delve deeper into their crystallization process, which, as a solid-state reaction, has been less investigated compared to the crystallization process of, most commonly used, solution-based methods. In this work, we employ spectroscopic ellipsometry, a non-destructive, high speed, and high accuracy characterization method, to study the real time annealing effect on thermally co-evaporated $CsPbI_2Br$ thin films in a temperature range between 25°C and 300°C. We achieve this by developing a singular dynamic model that can be fitted in real time as a function of temperature, providing insights into how thermal annealing influences the perovskite film's morphology and optical constants. Based on the latter, we derive the temperature dependance of the thermo-optic coefficient and Urbach energy, as well as analyze the interband transition energies via critical point analysis. We demonstrate that the γ- to β-phase transition can be identified through a pronounced shift in the bandgap energy, whereas the β- to α-phase transition can be discerned by a sharp increase in the film's roughness. We corroborate the obtained fit results with additional *in-* and *ex-situ* measurements, such as *in situ* grazing incidence wide angle X-ray scattering, atomic force microscopy, reflectance/transmittance, and profilometry.

2. Introduction

Metal halide perovskites have become a focus of major scientific research endeavors, owing to their excellent optoelectronic properties, such as high absorption coefficients, tunable bandgaps, large diffusion lengths, and defect tolerance[1–3]. These promising properties have been highlighted by the record-breaking efficiencies of perovskite-based solar cells[4–7]. Nonetheless, vigorous efforts are made to expand their application in other technologies, such as photodetectors[8,9], light-emitting diodes (LEDs)[10,11], and lasers[12]. So far, it has been found that hybrid organic-inorganic perovskites, where the A-site cation of the ABX_3 structure is a mixture of MA (CH_3NH_3), FA ($CH(NH_2)_2$), and Cs, are preferred for optimal performances[13]. However, despite their impressive power conversion efficiencies, hybrid organic-inorganic perovskites are sensitive to thermal degradation and thus not suitable for applications with a high thermal budget, either imposed by extrinsic (e.g. high ambient temperature, high temperature post processing) or intrinsic (e.g. triggering of self-heating mechanisms through resistive loses) factors[14–16].

The low thermal stability of hybrid perovskites is attributed to the presence of volatile organic cations, therefore all-inorganic perovskites, particularly ones in the $CsPbI_xBr_{3-x}$ ($0 \leq x \leq 3$) family, are emerging as a promising alternative[15]. $CsPbI_3$ has the lowest bandgap (~1.70 eV), making it an ideal candidate for solar cell and photodetector applications. At room temperature, bulk $CsPbI_3$ forms a stable yellow non-perovskite crystal structure (δ-phase) and requires temperatures above 320°C to form the perovskite black phase (α-phase)[17]. The black phase also includes the pseudocubic perovskite phases (β- and γ- phase), which emerge at lower temperatures. It is possible to kinetically trap the black phase at room temperature through rapid cooling, however, the yellow phase re-emerges almost instantaneously upon exposure to ambient moisture[18]. Increasing the Br content in the perovskite lattice has been found to help stabilize the black phase, with the compromise of increasing the film's bandgap ($CsPbBr_3$ has a bandgap of ~2.3 eV)[19]. For these reasons, $CsPbI_2Br$ is a commonly preferred composition for optoelectronic applications, such as visible light detection and multi-junction photovoltaics, since it combines a favorable bandgap (~1.91 eV) with improved black phase stability.

In terms of fabrication methods, vacuum thermal evaporation ensures conformal layer growth, paving the way for scalable and reproducible deposition of perovskite thin films[20]. Thermal evaporation of perovskite thin films can be achieved either via sequential evaporation[21] or via co-evaporation[9]. In the case of sequential evaporation, individual precursor layers are deposited, and the formation of the perovskite film occurs during a post-deposition annealing step. This step facilitates the precursor interdiffusion and reaction, leading to the formation of the perovskite structure[22]. In the case of co-evaporation, the precursors are evaporated simultaneously, rendering critical the precise control of their respective evaporation rates. A post-deposition annealing step is typically implemented to obtain the perovskite black phase and improve the film's crystallinity and homogeneity. A common implication of sequential deposition, which is inherently avoided with co-evaporation, is incomplete precursor intermixing[23]. For this reason, we focus on thermally co-evaporated $CsPbI_2Br$ thin films.

Despite recent strides, the performance of thermally evaporated perovskite-based optoelectronic devices still lags behind that of solution-processed ones[24]. This is primarily attributed to the fact that many optimization strategies for solution-processed perovskites, such as the introduction of

additives or macromolecular ligands to form 2D structures, are not applicable to the evaporation process[25]. To discover new optimization approaches, it is imperative to improve our understanding around the growth and crystallization mechanisms of thermally co-evaporated thin films. For example, only recently Dong et al. identified and explained the growth kinetic processes for obtaining stable γ-$CsPbI_3$ films without a post-deposition annealing step[26]. Besides the deposition conditions, the post-deposition annealing step has a great influence on the crystallinity and quality of the perovskite thin film. Therefore, these properties could be further optimized with insight obtained from *in situ* characterization techniques that have an acquisition time fast enough to detect the real-time annealing effect on perovskite thin films. A very powerful technique in this aspect is synchrotron-based grazing incident wide angle X-ray scattering (GIWAXS), which can provide information about crystal structure, grain morphology, phase transitions, and lattice strain[27]. However, in spite of its versatility and vast applications, access to GIWAXS synchrotron facilities is limited and costly. For more rapid advancements in the field, an alternative, more easily accessible *in situ* characterization technique would be pivotal.

In situ spectroscopic ellipsometry (SE) is a technique that fulfills these requirements and can be used to elucidate the real-time annealing effects on the thermally co-evaporated $CsPbI_2Br$ thin films. SE is a technique that measures a change in polarization as light reflects from or transmits through a material structure. The polarization change is represented as amplitude ratio, Psi (Ψ), and a phase difference, Delta (Δ)[28]. The unique advantage of SE is that it can provide both morphological and optical information, while at the same time being non-destructive and extremely fast. A few reports have already employed temperature-dependent *in-situ* ellipsometry on perovskite thin films to explore thermal-induced degradation or the effect of temperature on optical constants[29–32]. The knowledge of optical constants at various temperatures can be useful for multiple reasons, namely as an input: i) in DFT calculations, and ii) in optical simulations of photonic devices under actual operation conditions[14]. Nonetheless, none of the above-mentioned reports addresses thermally-evaporated perovskite thin films. On top of that, they offer no acknowledgment of morphological changes (e.g. thickness and roughness) during the heating or cooling process. This is because most reports on temperature-dependent *in situ* ellipsometry for perovskite thin films typically adopt a methodology where the sample is allowed to stabilize at each temperature increment for an extended period of time. This practice ensures adequate time for potential transitions or internal structure changes to occur, however it does not realistically represent the annealing conditions of a perovskite film during device fabrication and at the same time conceals information around real-time annealing effects.

In the present work, we propose a dynamic ellipsometry model that accounts for both morphological and optical variations of perovskite films as a function of time and temperature, with a focus on thermally evaporated $CsPbI_2Br$ films. Therefore, multiple mechanisms can be probed simultaneously, namely the lattice expansion and contraction, phase changes, grain coarsening, and consequent roughness increase, as well as the evolution of the optical constants and interband critical points. We corroborate the obtained model results with additional *in-* and *ex-situ* characterization measurements, such as synchrotron *in-situ* GIWAXS, atomic force microscopy (AFM), scanning electron microscopy (SEM), and Reflectance/Transmittance (R/T) measurements.

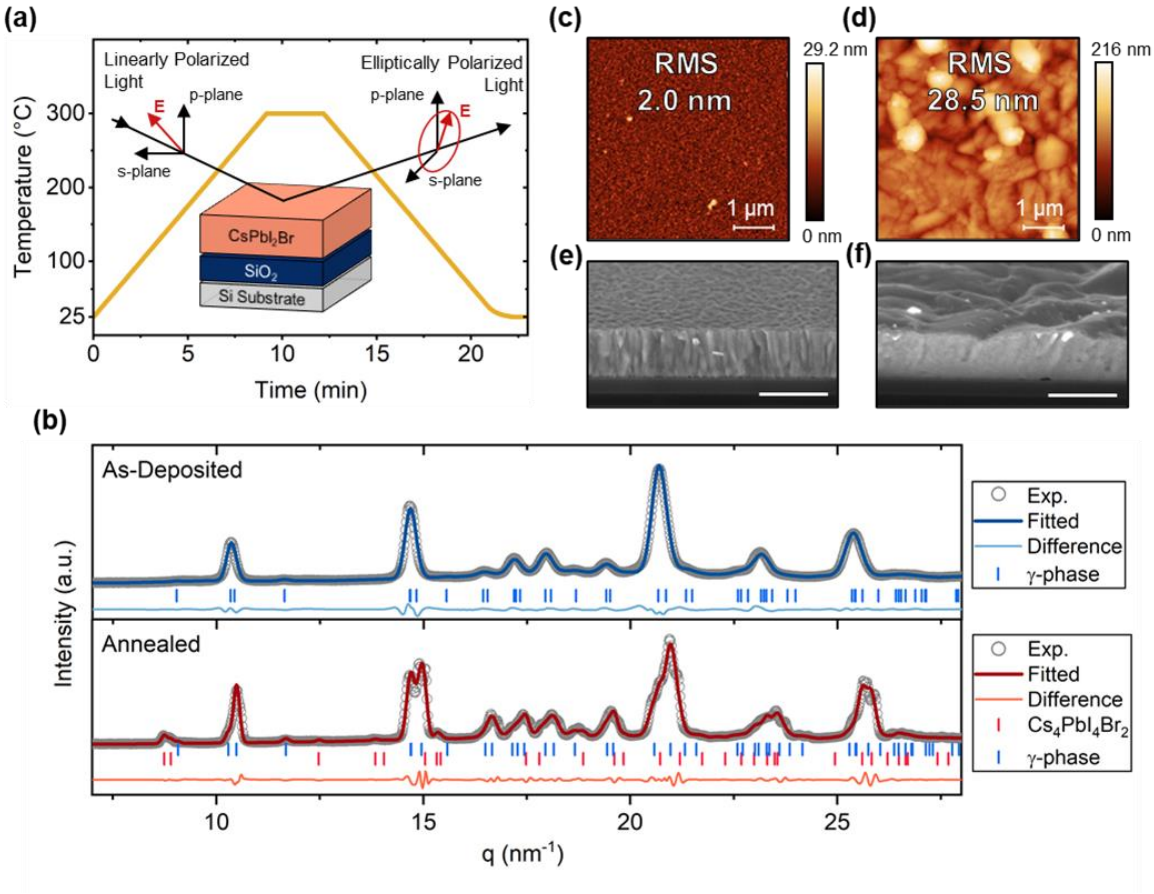

Figure 1. (a) Schematic illustration of the temperature-dependent *in situ* spectroscopic ellipsometry characterization measurement. (b) Comparison of 1D integrated GIWAXS signals from the measurement of the perovskite sample before (As-Deposited) and after (Annealed) thermal annealing. AFM image of the (c) As-Deposited state and (d) Annealed state. SEM cross-section of the (e) As-Deposited state and (f) Annealed state. The scale bar length for both is equal to 400 nm.

3. Results and Discussion

$CsPbI_2Br$ thin films were deposited via thermal co-evaporation of CsBr and PbI_2 precursors, according to the recipe described in the experimental section. The nominal CsBr:PbI_2 ratio was equal to 1.05:1.00, as it has been observed that an excess of Cs improves the ambient stability of the perovskite black phase without compromising the optoelectronic properties of the film[33]. Directly after deposition, one sample (deposited on Si/SiO_2 substrate) was subjected to the continuous heating ramp shown in **Figure 1a.** More precisely, the temperature was raised from room temperature (RT) to 300°C at a rate of approximately 30°C/min and allowed to stabilize for 3 minutes. The sample was then cooled down to RT with a rate of approximately 35°C/min. Concurrently with the heating/cooling ramp, SE measurements at a fixed angle of 70° were taken every 23 seconds. For this experiment, a Si substrate with 100 nm of thermally grown SiO_2 layer was deliberately selected to mitigate potential modeling complications arising from back-side reflections in semi-transparent substrates or multilayer interference within multilayer stacks. The sample was placed in an enclosed temperature stage that was continuously flushed with nitrogen.

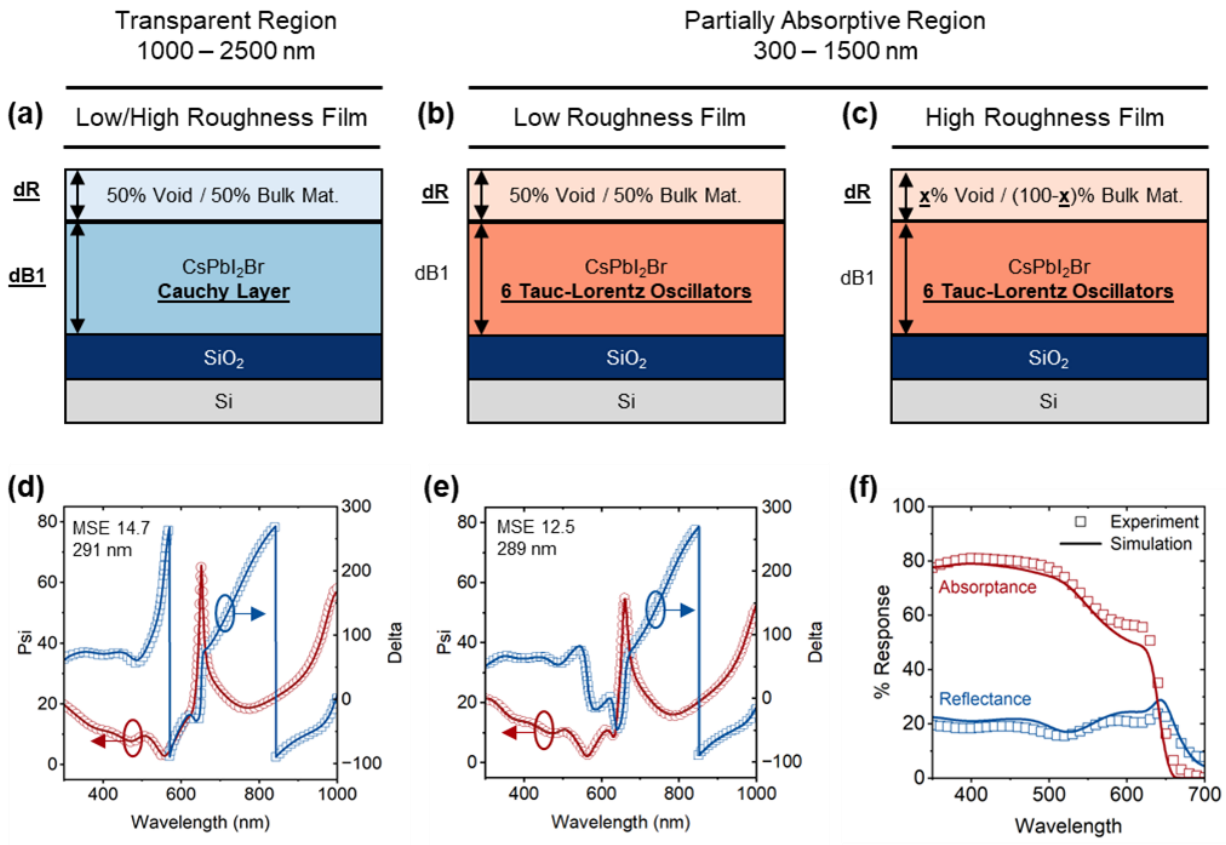

Figure 2. Overview of the developed SE models and accuracy of the fitting results. (a) – (c) Schematics of the optical models used for static ellipsometry fitting, depending on the transparency and roughness of the perovskite film. The bold and underlined text indicates the fitting parameters. For the models in the partially absorptive region, the bulk perovskite thickness (dB1) is fixed to the value calculated through the transparent region model. Comparison between the SE experimental (open symbols) and fitted results (solid lines) for (d) the As-Deposited state and (e) the Annealed state. (f) Comparison between the experimental (obtained through R/T measurements) and simulated (obtained with a transfer matrix algorithm and SE-derived nk values) spectra of Reflectance and Absorptance for the As-Deposited state.

It was deemed necessary to maintain proper alignment of the stage throughout the experiment, which required continuous minor manual adjustments. Hereafter, the initial state of the sample at RT will be denoted as "As-Deposited" and its final state at RT, after the completion of the thermal treatment, will be denoted as "Annealed".

Besides the SE measurement, we monitored an identical sample under the effect of the same heating ramp via *in situ* GIWAXS (more information in the Experimental Section). As revealed through GIWAXS in **Figure 1b**, the scattering profile of the As-Deposited state has been identified to match with the γ-$CsPbI_2Br$ phase. No secondary phases, such as PbI_2 or CsBr are observed, demonstrating the ability of thermal co-evaporation to provide pure γ-$CsPbI_2Br$ thin films, fully processed in RT. Other reports have discussed the low-temperature synthesis of γ-$CsPbI_3$ thin films through thermal co-evaporation, with the exception that they maintained the substrate temperature at 50°C during deposition[26,34]. The dominance of the black phase in our case, while keeping the substrate at RT, is attributed to the stabilizing effect of Br^-. **Figure S1** shows the film's phase

evolution with increasing temperature. The transition from the γ- (orthorhombic) to β-phase (tetragonal) is found to happen close to 130°C, while the transition to the α-phase (cubic) takes place at approximately 190°C. When the temperature of the heating ramp reaches 225°C, a new peak, at approximately 8.7 nm^{-1} appears. As further explained under **Figure S1**, this peak is attributed to the emergence of the 0D $Cs_4PbI_4Br_2$ phase, potentially formed due to the excess of CsBr during the co-evaporation process[35]. The 1D integrated GIWAXS signal for the Annealed state (bottom of **Figure 1b**) clearly indicates that considering two distinct perovskite phases, γ-$CsPbI_2Br$ and $Cs_4PbI_4Br_2$, allows us to account for all peaks in the diffraction pattern. To further explore potential structural differences of the film in the As-Deposited and Annealed state, we provide an overlayed comparison of the respective GIWAXS signals in **Figure S2**. These results indicate an almost doubling in crystallite size, as well as an increase of the macrostrain in the system.

Figure 1c and **Figure 1d** show the AFM images of the As-Deposited and Annealed state, respectively. The As-Deposited state shows particularly small grain sizes, with an average diameter of 30-40 nm, and an accordingly low root mean square (RMS) roughness, equal to 2 nm. This morphology is similar to what has been reported for as-deposited, thermally co-evaporated $CsPbI_xBr_{3-x}$ thin films[36,37]. Despite the small grain size, no pinholes are observed, as confirmed by the SEM cross-section in **Figure 1e**. After the thermal treatment and the subsequent temperature-induced grain coalescence, the surface of the Annealed state looks more compact, with a broad distribution of grain sizes (between 100 and 800 nm) and a significantly increased roughness (RMS value equal to 28.5 nm). This increase in film's roughness and grain size, which is further highlighted in the SEM cross-section of **Figure 1f**, is consistent with the GIWAXS results presented above, as well as with previous reports on co-evaporated $CsPbI_2Br$ films[38].To further evaluate the film quality in the As-Deposited and Annealed perovskite state, we performed Steady State Photoluminescence (SSPL) and Transient Photoluminescence (TRPL) measurements. **Figure S3a** compares the SSPL intensity for the As-Deposited and Annealed state. Evidently, the signal intensity for the Annealed state is almost 3 times higher than for the As-Deposited state. In order to investigate whether this increase could be related to the film's absorptance at the wavelength of the excitation laser (530 nm), we performed additional Reflectance/Transmittance measurements and calculated the film's Absorptance according to the formula A (%) = 100 – T (%) – R(%). The results are shown in **Figure S3b**. Indeed, the annealing process leads to a small increase in the Absorptance at 530 nm (from 71% to 74%), however this difference is not sufficient to explain the increase in PL intensity. Therefore, we conclude that this effect is mainly attributed to a reduction of the non-radiative recombination pathways through an improvement in the film's crystallinity. **Figure S3c** shows the normalized SSPL intensity for the As-Deposited and Annealed state and a weaker, longer wavelength peak is evident for the latter. This phenomenon was extensively studied by Schötz et al.[39] and was eventually attributed to a self-absorption mechanism, whose impact is intensified by strong internal reflections. We postulate that this explanation holds in our case, too, especially considering the increase in the film's surface roughness and the subsequent increase in light scattering. Lastly, **Figure S3d** shows the TRPL spectra for the As-Deposited and Annealed perovskite state. As further explained in the experimental section, a biexponential equation was used to describe the decay of both curves, yielding an average lifetime equal to 4 ns and 8 ns, respectively. These findings further highlight the reduction of defects in the film during the annealing process.

Static SE Model Development

To analyze the optical effect of the heating ramp on the thermally evaporated $CsPbI_2Br$ thin film we start by developing SE models for the already well-characterized As-Deposited and Annealed state. The process is quite standard and starts by limiting the SE data range to a spectrum where the perovskite is transparent, in this case between 1000 and 2500 nm. The bulk material of transparent films can be described by the empirical Cauchy dispersion model, which can be expressed as follows:

$$n(\lambda) = A + \frac{B}{\lambda^2} + \frac{C}{\lambda^4} \quad (1)$$

where A, B, and C are the fit parameters. The surface roughness is typically modeled by a Bruggeman Effective Medium Approximation (EMA) layer, which is a mixture of void and the bulk material in a 50:50 ratio, as introduced by Aspens et al.[40]. It is considered that the $SiO_2/CsPbI_2Br$ interface is entirely smooth, with no intermixing between the layers. As shown in **Figure 2a**, the fitting parameters in this range include the parameters of the Cauchy layer, as well as the thickness of the bulk and roughness layers. The relatively small number of fit parameters means that a good approximation of the bulk layer thickness (dB1) can be obtained, which is kept as a fixed parameter in the following steps. Consequently, the Cauchy layer is parameterized into a Kramers-Kroning consistent B-spline layer and the SE data range is extended to the visible spectrum, up to 300 nm. As a last step, the B-spline fitted dielectric constant is further parameterized by a general oscillator approach with multiple oscillators. In this work, we selected six Tauc-Lorentz oscillators to describe the complex optical constants of $CsPbI_2Br$, since increasing their number did not substantially improve the fitting accuracy. The schematic of this Tauc-Lorentz-based model is provided in **Figure 2b.**

The fitting accuracy is determined by the mean square error (MSE), a metric that quantifies the difference between the experimental and model-generated Ψ and Δ values, according to the following expression:

$$MSE = \sqrt{\frac{1}{2n-m}\sum_{i=1}^{n}\left[\left(\Psi_{exp} - \Psi_{mod}\right)^2 + \left(\Delta_{exp} - \Delta_{mod}\right)^2\right]} \times 1000 \quad (2)$$

where n is the number of (Ψ, Δ) pairs, m is the number of free parameters, and exp and mod refer to the experimentally measured data and theoretically modeled data, respectively[41].
As a rule of thumb, an MSE under 20 is usually necessary to guarantee a good match between our model and the actual optical parameters[42].

When following this protocol for the As-Deposited state, the developed model provided a fit with an acceptable MSE of 14.7, as shown in **Figure 2d**. The estimated thickness of 291 nm was consistent with the value provided by profilometry (295 nm, as shown in **Figure S4**). However, when following the same protocol for the Annealed state, the lowest MSE value that could be achieved was 29, showing a divergence between the experimental and simulated Ψ and Δ values (**Figure S5a**). It was possible to obtain a better fit (MSE 14) by setting the bulk thickness as a fitted parameter (**Figure S5b**), however the estimated perovskite thickness (309 nm) was not only

non-physical when compared to the thickness of the As-Deposited state, but also inconsistent with profilometry measurements (285 nm, **Figure S4**).

The challenge in obtaining a good SE fit for the Annealed state was attributed to its increased surface roughness. Specifically, there is a commonly overlooked limitation when using a Bruggeman EMA layer to model a film's surface roughness. A single EMA layer can adequately describe the surface roughness only when the dimensions of the roughness structures (D) are much smaller than the wavelength (λ) of the SE light probe and the condition of $D < 0.1\ \lambda$ needs to be satisfied[28]. When D exceeds this limit, a complex EMA-multilayer model is generally necessary for the SE analysis[43]. Underestimating the sample's roughness can have a significant impact on the estimated dielectric constants of solar cell materials, as it was demonstrated by Fujiwara et al.[44]. In the case of our thermally evaporated $CsPbI_2Br$ thin films, if we consider that D is equal to the AFM-estimated RMS roughness and that the SE light wavelength is between 300 and 2500 nm, we see that the surface roughness of the As-Deposited state ($D \sim 2$ nm) is well below the 0.1λ threshold. On the other hand, the Annealed state ($D \sim 29$ nm) is right on the limit, which could explain the difficulty in obtaining an acceptable MSE. To overcome this issue, we keep the bulk layer thickness as a fixed parameter and set the percentage of voids in the roughness layer as a fit parameter, as shown in **Figure 2c**. Indeed, with this change, we can obtain an MSE equal to 12.5 without resorting to more complicated modeling approaches, such as the multi-layer EMA approach. A complete overview of the aforementioned models and their respective fitting results is provided in **Table 1.**

State	Model	MSE	Bulk Thickness (nm)	Roughness Thickness (nm)	% Voids
As-Deposited	Fixed Thickness Fixed % Voids	14.76	291.6	3.68 ± 0.11	50
Annealed	Fixed Thickness Fixed % Voids	29.07	289.0	9.68 ± 0.23	50
	Fitted Thickness Fixed % Voids	14.05	309.9 ± 0.43	7.65 ± 0.13	50
	Fixed Thickness Fitted % Voids	12.54	289.1	20.05 ± 0.25	16.3 ± 0.34

Table 1. Summary of the developed SE models for the fitting of the experimental data for the As-Deposited and Annealed perovskite state. The As-Deposited state was accurately described by a model with fixed bulk thickness (derived in the transparent region) and a roughness layer with 50% voids. The best way to describe the Annealed state was found to be a model with fixed bulk thickness and fitted percentage of voids in the roughness layer.

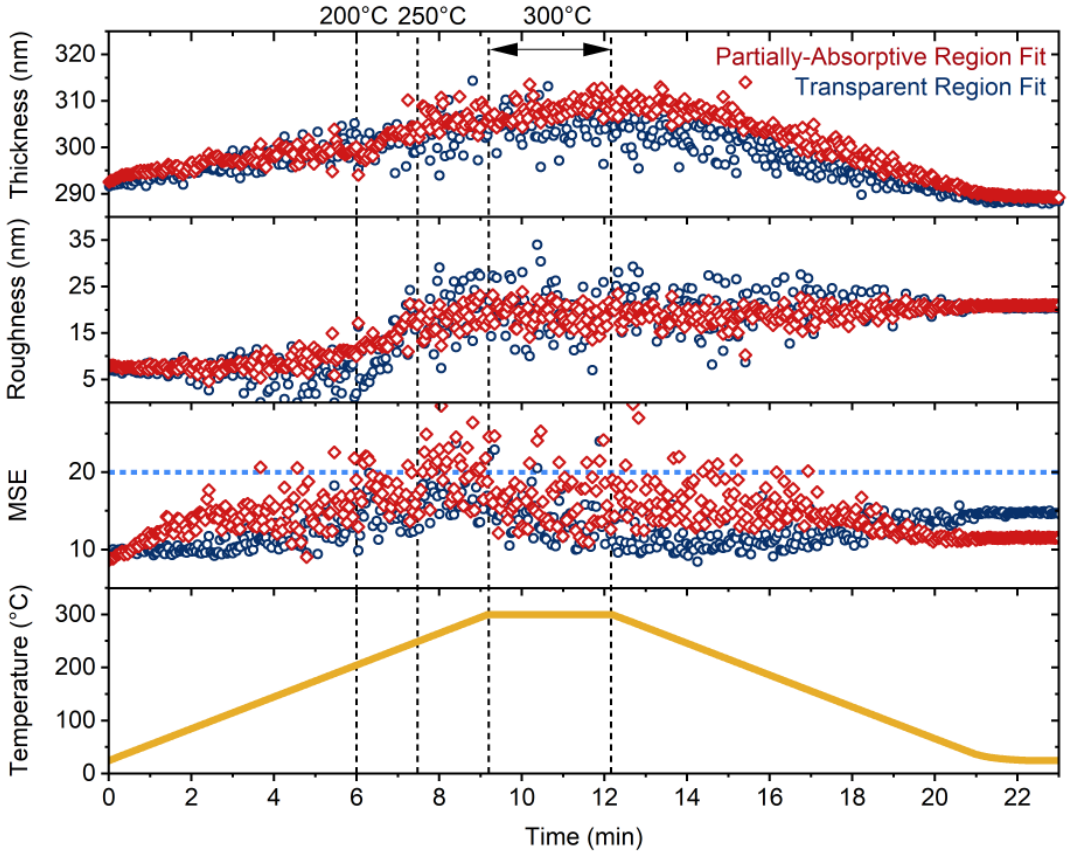

Figure 3. Evolution of the $CsPbI_2Br$ film's thickness and roughness, as well as the fit's MSE, as a function of time and temperature according to our dynamic SE model. The blue scatter points indicate the fit results of a Cauchy-based model (as the one shown in Figure 2a) in the transparent region (1000 – 2500 nm). The red scatter points indicate the fit results of the dynamic Tauc-Lorentz-based model (as the one shown in Figure S4) in the partially absorptive region (300 – 1000 nm). The vertical line labeled as 210°C indicates the point the layer's roughness starts to increase, while the vertical line at 250°C indicates the completion of this effect. The horizontal blue line in the MSE graph is a rule of thumb for the highest acceptable MSE that can guarantee a good match between the experimental and fit results.

To confirm the accuracy of our SE analysis, we extract the optical constants of the As-Deposited and Annealed state and simulate the expected reflectance and absorptance using the transfer matrix algorithm. We compare the simulated spectra with the respective experimental values. The comparison for the As-Deposited and Annealed state is shown in **Figure 2f** and **Figure S6**, respectively. In both cases, there is a good match between the experimental and simulated values, underlining the accuracy of our SE fitting. It has to be noted that within the absorptance and reflectance spectra of the Annealed state, no discernible feature can be attributed to the presence of the 0D $Cs_4PbI_4Br_2$ phase, as detected by GIWAXS. This is in agreement with what was reported by Bai et al.[35], who were able to detect a peak attributed to Cs_4PbI_6 in the absorptance spectrum of $CsPbI_3$ thin films only when the ratio between CsI and PbI_2 was increased to 1.6:1.0. This ratio is much larger compared to the CsBr:PbI_2 ratio we use during the deposition of our films.

Dynamic SE Model Development

Having established the accuracy of our SE model for the As-Deposited and Annealed state, we move to the dynamic modeling of the sample under the effect of the heating and the cooling ramp. It is known that SiO_2 has a very low thermal expansion coefficient, as low as 0.5×10^{-6} K^{-1}, especially when compared to the thermal expansion coefficient of lead-iodide-based perovskites (50×10^{-6} K^{-1})[18]. For this reason, both the thickness and the optical constants of the SiO_2 layer were considered as fixed parameters in the dynamic SE model. Rather than adopting a method that depends on creating multiple static models at different temperature intervals, we develop a singular dynamic model that can be fitted in real-time, describing aspects of the optical, morphological, and structural evolution of the $CsPbI_2Br$ thin film.

As shown in **Figure S7**, this dynamic model is a mixture of perovskite states at different timestamps/temperatures, whose optical constants (derived according to the methodology of the previous section) are fixed while their volume fraction is a fitted parameter. Specifically, this mixture contains the As-Deposited state (t = 0 min), the Annealed state (t = 23 min), as well as the perovskite state at the highest temperature point, i.e. 300°C (t =11 min). On top of that, a closer inspection of Ψ and Δ as a function of time and temperature (**Figure S8**) shows that a major shift is happening between the 5th and 7th minute of the experiment. Therefore, we include those two states (t = 5 min and t = 7 min) in the mixture, as well. These five states proved to be sufficient to describe the complete evolution of the perovskite layer, as will be further discussed later. Adding more states in the mixture, such as a state during the cooling of the sample (between the 11th and 23rd minute of the experiment) did not lead to a reduction of the MSE. Besides the volume fraction of each state, additional fit parameters were the thickness of the bulk and roughness layer. In order to minimize the number of fitting parameters, we fixed the percentage of voids in the roughness layer to 15% for all states, as it could consistently provide a good fit for both the low-roughness (As-Deposited) and high-roughness (Annealed) states.

The results of the dynamic fit are presented in **Figure 3**, which shows the evolution of the film's thickness and roughness as a function of time, as well as the overall MSE. The MSE is mostly maintained below 20 for the whole duration of the experiment, which is a good indication of the accuracy of our model, however, this metric alone does not guarantee its physicality. Instead, to evaluate the physicality of the dynamic EMA model we compare the results it provides in the partially absorptive region (300 – 1000 nm) with the results of a simpler dynamic Cauchy-based model in the transparent region (1000 – 2500 nm). The Cauchy-based dynamic model is more sensitive to thickness variations because a transparent film enables the detection of light that is reflected both from the top surface of the film, as well as from the interface between the film and the substrate. At the same time, the SE light wavelength in the transparent region is much larger than the dimensions of the roughness structures, therefore the simulation of the roughness layer becomes less complicated. For all these reasons, the nearly identical morphological trends exhibited by the Dynamic EMA model and the Dynamic Cauchy model strongly validate the physicality of the former. Despite the phase changes occurring during the heating and cooling of the sample (**Figure S1**), the film's thickness exhibits a linear correlation with temperature. This observation aligns with what has already been reported for $CsPbI_3$ thin films, whose normalized cell volume varies linearly with temperature while transitioning sequentially from the α- to β- and to the γ-phase[45].

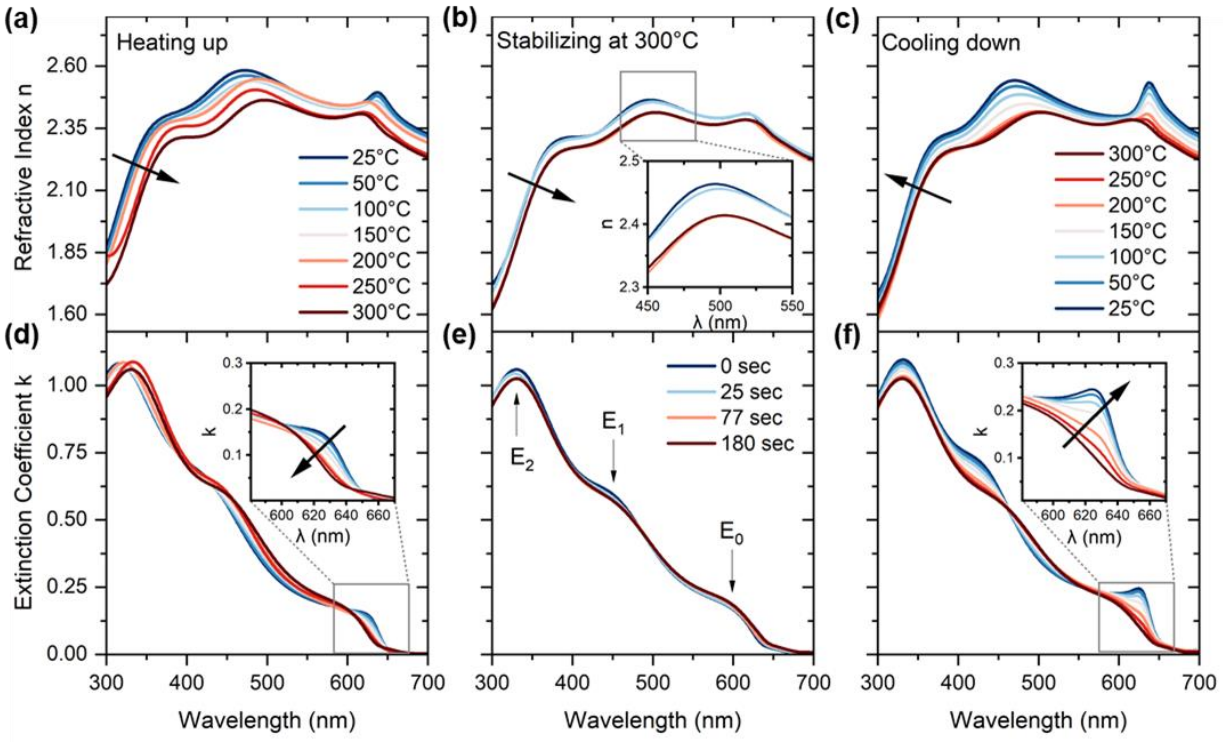

Figure 4. Evolution of the $CsPbI_2Br$ film's refractive index n during the (a) heating up to 300°C, (b) stabilizing at 300°C, and (c) cooling back down to room temperature process. The overall decrease of the refractive index with increasing temperature is know as the perovskite's negative thermo-optic coefficient. The inset in (b) highlights a hysteresis between the attainment of a temperature point and the plateauing of the refractive index. Evolution of the $CsPbI_2Br$ film's extinction coefficient k during the (d) heating up to 300°C, (e) stabilizing at 300°C, and (f) cooling back down to room temperature process. The insets in (d) and (f) highlight that the absorption edge of the perovskite gradually becomes less steep with increasing temperature. This is associated with a rise in the Urbach energy.

In terms of the film's roughness, its value remains almost constant (between 5 and 10 nm) for the first 6 minutes, until approximately 200°C, after which there is a sharp increase before it stabilizes again at a value close to 20 nm. It needs to be highlighted that this value represents the thickness of the roughness layer we use in our SE model, which is different from, for example, the RMS roughness we get during an AFM measurement. However, considering that this roughness value is directly related to the grain size and morphology, it is possible to extract relevant information. Specifically, it is indicated that the grain morphology does not significantly change until a specific temperature point is reached (in this case approximately 200°C). To further evaluate this point, we anneal two $CsPbI_2Br$ samples for 3 minutes at 180°C and 250°C, with the respective AFM scans

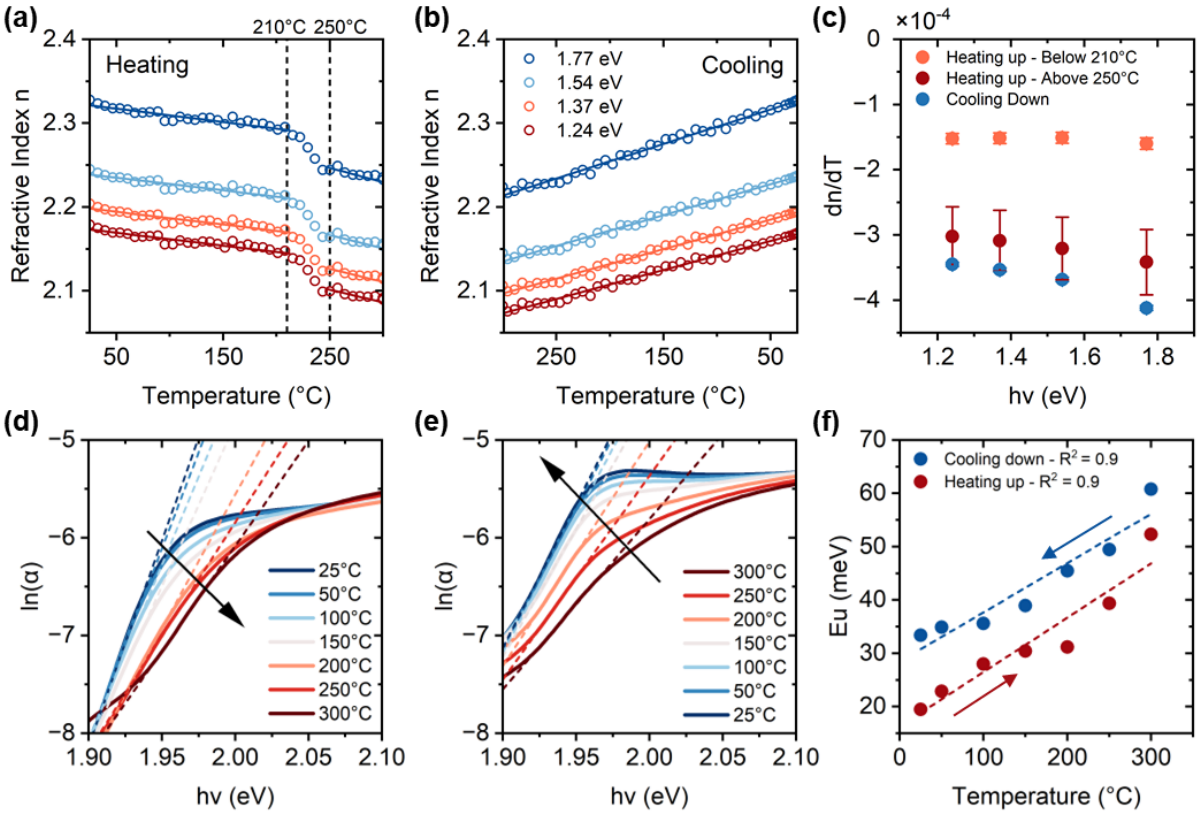

Figure 5. Temperature dependance of the refractive index of a $CsPbI_2Br$ thin films for smaller than the fundamental bandgap photon energies during (a) the heating and (b) cooling process. The solid lines indicate the fit of a linear function, and their slope is used to estimate the (c) Thermo-optic coefficient of $CsPbI_2Br$. The error bars reflect the error of the linear fit in Figure 5a and 5b. Temperature dependence of absorption edge, expressed through the natural logarithm of the absorption coefficient during (d) the heating and (e) the cooling process. The dashed lines indicate the fit of a linear function, and their slope is used to calculate the (f) Urbach energy as a function of temperature during the heating and cooling process, according to **eq. 3**.

shown in **Figure S9a** and **Figure S9b**. It is indeed confirmed that when the temperature is maintained below 200°C, the average grain size remains below 150 nm, while when the annealing temperature exceeds 200°C, the average grain size immediately increases to a range between 400-800 nm. This abrupt shift in crystallite size could be attributed to the transition from the tetragonal to the cubic phase. Through the ellipsometry data, it is also indicated that once this transition is completed, extending the annealing duration does not have a further impact on the film roughness. To test this hypothesis, we submit a new sample to the same heating ramp as the one in Figure 1a, with the difference of extending the dwelling time at 300°C from 3 minutes to 15 minutes. The respective film surface morphology is shown on **Figure S9c** and **Figure S9d**, where indeed only a minor increase in the RMS roughness (from 28.5 nm to 31.6 nm) is observed.

Figure 4 shows the evolution of the film's optical constants, the refractive index (n) and the extinction coefficient (k), during heating up from RT to 300°C (**Figure 4a** and **Figure 4d**), stabilizing at 300°C (**Figure 4b** and **Figure 4e**), and lastly cooling back down to RT (**Figure 4c** and **Figure 4f**). The are various changes taking place with increasing temperature, such as (i) an overall decrease of the refractive index, (ii) the slope of the absorption edge becoming less steep,

and (iii) an energy shift of the excitation peaks. All these changes, as well as the underlying physical mechanisms, will be further discussed in the paragraphs below. It is important to highlight at this point that this characterization measurement aims to observe the real-time effects of thermal annealing on evaporated $CsPbI_2Br$ thin films. For this purpose, we implement a continuous and relatively fast heating ramp (~30°C/min). This approach is anticipated to induce a hysteresis between the attainment of a temperature point and the completion of any potential transitions or internal structure changes. This is more effectively showcased in the inset of **Figure 4b**, where a shift at the value of n is observed, while the temperature is stable at 300°C. Specifically, a slight decrease in the refractive index is observed after 77 seconds at 300°C, while prolonging the exposure to this temperature point shows no discernible additional effect on the optical response of the perovskite thin film.

Thermo-Optic Coefficient Analysis

To begin with, it can be observed in **Figure 4** that as the temperature of the perovskite film increases, its overall refractive index decreases, and vice versa. The dependence of the refractive index on temperature is known as the thermo-optic coefficient (dn/dT), which has been reported to be negative for hybrid organic-inorganic perovskites[14] and quasi-2D perovskites[46]. Here we report that all-inorganic perovskites have a negative thermo-optic coefficient, as well. This stands in contrast to most conventional inorganic semiconductors (such as Si[47], Ge[48], GaN[49] etc) which are known to have a positive thermo-optic coefficient. Handa et al. attributed this unique characteristic of perovskites partially to the blueshift of resonance energy with increasing temperature, but mainly to their large thermal expansion coefficient and the consequent decrease in the valence electron density[50]. The variation of the refractive index at specific sub-bandgap energies as a function of temperature is shown in **Figure 5a** and **Figure 5b** for the heating and cooling stages, respectively. During the heating stage, n varies linearly with temperature, until 200°C, when a sharp, discontinuous transition is observed. This transition is completed at around 250°C. During the cooling stage, n maintains its linear relationship to temperature. The thermo-optic coefficient for these stages is obtained through a linear fit, with the corresponding results shown in **Figure 5c**. The thermo-optic coefficient values reported here (between -1.5 and -4.5 × 10^{-4} K^{-1}) are close to the value that has been previously reported for $MAPbCl_3$ (-3 × 10^{-4} K^{-1} at 430 nm)[14]. It is interesting to observe that the discontinuity in the thermo-optic coefficient during the heating ramp coincides with the onset of the film's roughness increase (shown in **Figure 3b**), which starts at 200°C and is completed at approximately 250°C. This correlation can be justified if we consider that the thermo-optic coefficient is mainly determined by the expansion of the lattice[50] and that the roughness increase in a SE model is implemented through a thickness increase of the respective layer.

Urbach Tail Analysis

Moving on to the effect of temperature on the perovskite's extinction coefficient, shown in **Figures 4d-f**, it can be observed that the slope of the absorption edge is becoming less steep with increasing temperature, and vice versa. This is illustrated more clearly in the insets of **Figure 4d** and **Figure 4f**. The slope of the absorption edge is related to sub-bandgap absorption tails, defined as densities of states that extend from the bands into the bandgap of a photoactive layer[51]. The slope is quantified by the Urbach energy (E_U)[52], which, in other words, describes the energetic disorder at the band edge[53]. This is why small E_U values are indicative of a material's high structural quality, further translating into superior electronic properties, such as reduced recombination[51] and high

carrier mobility[54]. Previous studies have already explored the temperature dependence of Urbach energy for perovskite thin films and crystals, such as $CH_3NH_3PbI_3$[51,54–56] and $CsPbBr_3$[57]. The most used characterization measurements include photothermal deflection spectroscopy, Fourier transform photocurrent spectroscopy, as well as time-integrated and time-resolved photoluminescence measurements. These studies have primarily focused on temperatures from RT and below. Our study, on the other hand, employes SE for the investigation of the E_U temperature dependence for perovskite films, broadening, at the same time, the temperature range from RT up to 300°C. Expanding the temperature range holds high relevance considering the direct correlation between Urbach energy and critical parameters such as the open circuit voltage (V_{OC}) in solar cells[54], and consequently, the dark current in photodiodes.

The Urbach energy can be obtained through the empirical relation:

$$a(h\nu) = a_0 \exp\left(\frac{h\nu}{E_U}\right) \quad (3)$$

where a is the absorption coefficient, a_0 is a constant, $h\nu$ is the photon energy, and E_U is the Urbach energy. Therefore, based on the extinction coefficient k, we calculate the natural logarithm of the absorption coefficient ($ln(a)$) for specific temperature points during the heating and cooling stages (**Figure 5d** and **Figure 5e**, respectively), allowing us to obtain the Urbach energy as a function of temperature. The results are shown in **Figure 5f**. It can be observed that E_U increases linearly with temperature. This dependence can be described by the formula[58]:

$$E_U(T) = E_U(0) + \frac{2E_U(0)}{e^{\frac{\theta_E}{T}}-1} \quad (4)$$

The first term in this equation, $E_U(0)$, is temperature-independent and constitutes the static component of E_U, i.e. its value scales with intrinsic disorder of the material. The second term in the equation is the dynamic component of E_U (i.e. it is temperature dependent) and describes the phonon contribution to the measured value of E_U. T is the absolute sample temperature and θ_E is the Einstein phonon temperature. Static disorder dominates at temperatures below 150 K, so the trend presented here is mostly determined by dynamic disorder and exciton-phonon interactions[51].

The E_U value for the As-Deposited state at RT is approximately 19 meV, which suggests a well-ordered microstructure and is consistent with what has been previously reported for solution-processed perovskite thin films. Notably, the Annealed state at RT shows a 14 meV increase, with E_U becoming equal to ~33 meV, despite the improvements in crystallinity and preferential orientation that were discussed above. Considering that both measurements are done at RT, the increase in E_U can only be explained by an increase in the value of the static term $E_U(0)$, i.e. an increase in the structural disorder. This increase could be attributed to temperature-induced strain in the lattice[59], which is also indicated as peak splitting at the GIWAXS data presented in **Figure 1b**. As to what regards the *in situ* E_U temperature dependence, we observe an almost linear behavior. Studying the E_U temperature dependence of $CH_3NH_3PbI_3$ films, Singh et al.[55] were able to identify two different slopes for the orthorhombic and tetragonal phase, however, the difference was only minor without any sharp discontinuities. Unlike their approach, in our case, we implement a continuous heating ramp, without stabilization intervals, leading to a more gradual transition and potential co-existence of phases. Therefore, we avoid attributing the variations in the scattering profile of E_U to specific structural transitions.

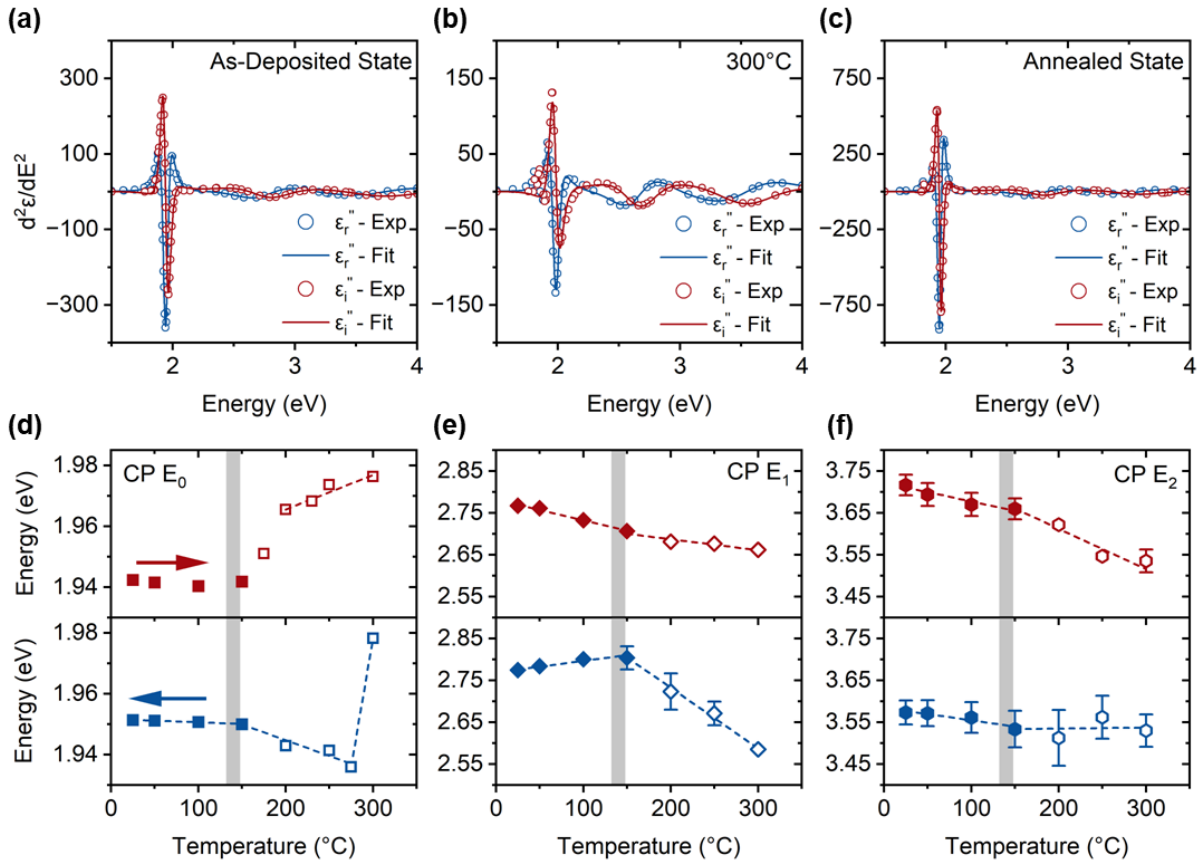

Figure 6. Second derivatives of the real and imaginary parts of the dielectric function and the fitted values for the (a) As-Deposited state, (b) the state at 300°C, and (c) the Annealed state. The number of scatter points for the experimental results has been reduced for cleared visual representation. (d)-(f) Temperature dependence of the interband critical point energies (E_0, E_1, E_2) of $CsPbI_2Br$ during the heating (red scatter points) and cooling (blue scatter points) process. The gray shaded area depicts the temperature transition region between the orthorhombic (filled scatter points) and tetragonal (empty scatter points) phase. The error bars reflect the error in the fitting of **eq. 5** to the experimental data.

Critical Point Analysis

For the last part of our analysis, we focus on the position and temperature-induced shift of the peaks that are distinguished in both the refractive index and the extinction coefficient values depicted in **Figure 4**. These peaks are clearly labeled in **Figure 4e**, as E_0, E_1, and E_2, and correspond to interband transitions at high-symmetry k-points of the Brillouin zone according to previous density function calculations[30]. For an α-$CsPbI_2Br$ film, E_0 is the fundamental direct bandgap and is caused by the interband transition from the valence band maximum (VBM) to the conduction band minimum (CBM) at the R point in the first Brillouin zone. Specifically, the fundamental bandgap E_0 is defined by antibonding Pb and halogen orbitals and can be influenced by the lattice's expansion or by the tilting of the [PbX_6^{4-}] octahedra[60]. E_1 is the direct bandgap mainly caused by the interband transition at the M point in the Brillouin zone and is attributed to transitions from the 6s to 6p orbits in the Pb^{2+} sublattice. Lastly, E_2 is caused by the interband transition at the X point of the Brillouin zone and is considered a doublet transition owning to the charge-transfer transitions from the I/Br 3p/4p valence to the Pb 6p conduction bands[41].

To accurately assign the energies of these interband transitions, as well as their temperature dependence, we perform a critical point (CP) analysis. Through our SE model, we obtain the real and imaginary parts of the material's dielectric function (ε_r and ε_i), and followingly we calculate their second derivative in order to enhance the structural features in the spectra. These derivatives are then fitted simultaneously with a function that is the sum of several CPs, each of them described by the equation:

$$\frac{\partial^2 \varepsilon}{\partial \omega^2} = n(n-1)Ae^{i\Phi}(\omega - E + i\Gamma)^{(n-2)} \quad (5)$$

where A, Φ, E, Γ, and n are resp. the amplitude, phase, energy position, broadening, and the dimensionality of the CP. In this analysis, we account for $n = -1$, which has been previously used to describe the excitonic nature of the optical transitions in perovskites[29,61]. The second derivates and the fit results for the As-Deposited and Annealed state, as well as the state at 300°C are presented in **Figures 6a-c**, demonstrating a good match between the experimental and fitted values.

Figure 6d-f show the CP's energy as a function of temperature during the heating and cooling process, calculated according to **eq. 5**. The value of the fundamental bandgap (E_0) at RT (1.94 – 1.95) is in agreement with what has been previously reported [30,62–65]. Overall, an increase in temperature is causing a blueshift for E_0 and a redshift for E_1 and E_2. These trends are in complete agreement with what has been previously observed for $CsPbBr_3$ single crystals through temperature-dependent SE measurements[61]. The blue shift of E_0 has been mainly attributed to the increase in inter-atom distance due to thermal expansion, leading to the large lowering of the valence band maximum[66]. It can also be observed that at around 140°C all CP energies display a discontinuity versus temperature. This is the temperature point where, according to our GIWAXS analysis (**Figure S1**), the transition between the orthorhombic and tetragonal phase is taking place. The discontinuity in CP's energy around this transition was observed for $CsPbBr_3$ single crystals, as well[60]. On the other hand, the transition between the tetragonal and cubic phase was reported to be continuous without any sharp characteristics. This is further corroborated for $MAPbI_3$ through DFT calculations, claiming that the tetragonal to cubic phase transition is characterized by a continuous tilting of the PbI_6 octahedra, as well as the continuously changing temperature-dependent Pb-I bond lengths[67]. One outlier from the described trends is the energy variation of CP E_0 during the cooling process, which exhibits a sharp decline upon initiation of the sample's cooling. This feature needs to be further investigated.

4. Conclusions

In conclusion, we have reported the development of a dynamic spectroscopic ellipsometry model that was used to monitor the real-time annealing effect on thermally co-evaporated $CsPbI_2Br$ thin films. We have emphasized the importance of considering the perovskite layer's roughness for acquiring accurate results. Through corroborating the simulated results with additional characterization measurements, we have proved that a mixture layer consisting of the perovskite state at five different timestamps is sufficient to describe the complete evolution of the film during

the annealing process. On the second part of this work, we utilized the simulated results to further explore the temperature-dependent properties of all-inorganic $CsPbI_2Br$ thin films. Specifically, we have identified that the transition from the orthorhombic (γ-) to the tetragonal (β-) phase can be recognized through a sharp discontinuity in the energy position of the film's critical points, while the transition from the tetragonal (β-) to the cubic (α-) phase coincides with a sharp increase in the film's roughness. Lastly, we have provided an analysis of relevant for the performance of perovskite-based device parameters, such as the thermo-optic coefficient and the Urbach energy. As a future perspective, we believe that the presented dynamic modelling approach for temperature-dependent SE spectra can be used to further explore the effects of the substrate, including different transport layers, on the growth and crystallization of thermally evaporated perovskite layers. It is highly recommended to first perform a temperature-dependent SE study on the transport layer alone to determine whether its optical properties can be considered temperature-independent. If they cannot, such as in the case of organic transport layers with large thermal expansion coefficients, an additional dynamic model should be developed to describe that layer.

5. Experimental Section

Perovskite Deposition: $CsPbI_2Br$ thin films were thermally evaporated from CsBr (abcr, ultra dry; 99.9%) and PbI_2 (TCI Chemicals, >98%) precursors using a Kurt J. Lesker SPECTROS system. Approximately 1 gr of material was loaded into the crucible of each source. The evaporation rates were calibrated by separately depositing CsBr and PbI_2 films on Si/SiO_2 substrates and measuring their respective thickness with *ex-situ* ellipsometry (RC2 J.A. Woolam). For a co-evaporated, stoichiometric film, the precursor thickness ratio (TR) should be equal to $TR = \frac{Molar\ Mass\ (A)\ /\ Density\ (A)}{Molar\ Mass\ (B)/\ Density\ (B)}$, where A and B indicate the two precursors. Based on this assumption, and aiming for a moderate total evaporation rate of ~0.8 Å/s and a 1.05:1.00 CsBr to PbI_2 molar ratio, the evaporation rates for CsBr and PbI_2 were set at 0.32 Å/s and 0.47 Å/s, respectively. The shutter, which prevents the deposition of material on the substrates, was removed only after both deposition rates were stable and the duration of the deposition was tuned to obtain $CsPbI_2Br$ film with a nominal thickness of 275 nm. During deposition, the temperature of the two sources was continuously and automatically adjusted to ensure constant evaporation rates, while the substrate holder, which could be loaded with up to nine samples, was rotating to ensure high uniformity. The substrate holder was kept at room temperature during the deposition.

In situ Spectroscopic Ellipsometry was performed using an RC2 Ellipsometer by J.A. Woolam, equipped with a Linkam THMS600 Temperature Stage. A 275 nm $CsPbI_2Br$ layer was deposited on Si substrates with 100 nm of SiO_2. The samples were transferred from the fabrication glovebox to the ellipsometer in a container filled with nitrogen and were only briefly exposed to open air while being loaded on the temperature stage. Thereafter, the stage was continuously flushed with nitrogen. Due to the optical windows of the heating cell, the ellipsometer angle of incidence was fixed at 70°. After fixing its height and alignment, that stage was heated up to 300°C with a rate of approximately 30°C/min. One ellipsometry measurement in the range of 210 – 2500 nm was taken every 23 seconds. Once the target temperature of 300°C was reached, it was sustained for 3 minutes. The stage, which was connected to a Liquid Nitrogen Dewar, was then cooled down back

to room temperature at an approximate rate of approximately 35°C/min. The modeling and fitting of the experimental results were done with J.A. Woolam's CompleteEASE software.

In situ GIWAXS: An identical sample was submitted to *in situ* synchrotron GIWAXS under the effect of the same heating ramp. Temperature-dependent GIWAXS data were collected under N_2 environment at NCD-SWEET beamline, located at the ALBA synchrotron in Cerdanyola del Vallès, Spain. A monochromatic X-ray beam with a wavelength (λ) of 0.9574 Å and dimensions of 80 × 30 μm^2 (horizontal × vertical) was used for data acquisition, utilizing a Si (111) channel cut monochromator and a set of CRLs to collimate the X-ray beam. The scattered signal was precisely captured by a Rayonix LX255-HS area detector. To accurately determine the reciprocal q-space and sample-to-detector distance, Cr_2O_3 from NIST was utilized as a calibrant. For full penetration of the X-ray beam through the layer, an incident angle (α_i) of 1° was deliberately chosen. Throughout the data acquisition process, a continuous flow of N_2 was maintained over the sample. The sample temperature was controlled using a Linkam® THMS600 device (0.01ºC accuracy) adapted for grazing incidence measurements. To analyze the collected two-dimensional (2D) images, azimuthal integration was performed using PyFAI[68], a reliable software tool. Subsequently, the resulting unit cell models were refined using the Le Bail method implemented in Fullprof[69], a comprehensive analysis software.

Further Film Characterization Measurements: AFM images were obtained using a Bruker Dimension Edge system to evaluate the film's grain size and roughness; the measurements were carried out in air. The thickness of the samples was corroborated through profilometry measurements in open air using the DektakXT Stylus Profiler. For the experimental evaluation of the Reflectance and Transmittance spectra, 275 nm $CsPbI_2Br$ films were deposited on soda lime glass substrates. The measurements were carried out using a Bentham PV300 Spectral Response system. A light beam from a 500 W Xenon source was coupled into a Bentham MSH-300 monochromator, giving coverage over the spectral range of 350 – 1800 nm. A silicon photodiode with a known responsivity was used for calibration. The reflectance and transmittance measurements were executed in open air using a DTR6 integrating sphere with a spectral range from 350 to 700 nm. The absorptance was then calculated using the formula A(%) = 100 – T(%) – R(%). The simulated values of the Reflectance and Transmittance spectra were obtained with the transfer matrix algorithm[70] using the SE-derived optical constants of the As-Deposited and Annealed state. $CsPbI_2Br$ films, deposited on soda lime glass substrates, were used for the SSPL and TRPL measurements. The measurements were carried out using a Hamamatsu Quantaurus-Tau Fluorescence lifetime spectrometer. The excitation light intensity was fixed at 0.1 mW. A 530 nm and 645 nm laser wavelength was used during the SSPL and TRPL measurement, respectively. The biexponential equation $I_{PL}(t) = A_1 exp\left(-\frac{t}{\tau_1}\right) + A_2 exp\left(-\frac{t}{\tau_2}\right) + y_0$ was used to describe the decay in the TRPL data. Followingly, the carriers' average lifetime was calculated using the equation $\tau_{avg} = \frac{A_1 {\tau_1}^2 + A_2 {\tau_2}^2}{A_1\tau_1 + A_2\tau_1}$.

Supporting Information:

- *In situ* and *ex situ* reduced 1D GIWAXS data; SSPL and TRPL spectra for the As-Deposited and Annealed state; profilometry measurements; additional ellipsometry fitting results and Reflectance/Transmittance measurements for the Annealed state; in situ Ψ and Δ evolution; schematic of dynamic optical model; additional AFM scans

Acknowledgement:
We acknowledge the financial support from the Fund for Scientific Research Flanders (FWO) under Project number S004322N (GigaPixel). GIWAXS experiments were performed at BL11 NCD-SWEET beamline at ALBA Synchrotron with the collaboration of ALBA staff. This work is supported by Internal Funds KU Leuven (C14/23/090) and the KU Leuven Research fund (iBOF-21-085 "PERSIST").

Data Availability:
All the data that support the findings of this study are available from the corresponding authors upon reasonable request.

Author Information:

Corresponding Author

Athina Papadopoulou[1,2]*
E-mail: athina.papadopoulou@imec.be

Jan Genoe[1,2]*
E-mail: jan.genoe@imec.be

[1]imec, Kapeldreef 75, 3001 Leuven, Belgium
[2]Department of Electrical Engineering (ESAT), KU Leuven, Kasteelpark Arenberg 10, 3001 Leuven, Belgium

Table of Contents Figure

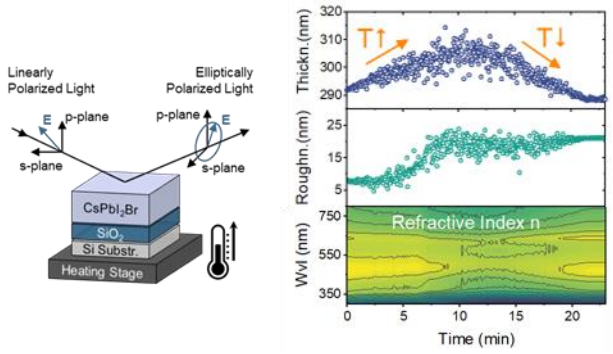

6. Bibliography

1. Burschka, J. *et al.* Sequential deposition as a route to high-performance perovskite-sensitized solar cells. *Nature* **499**, 316–319 (2013).
2. Heo, J. H. *et al.* Efficient inorganic-organic hybrid heterojunction solar cells containing perovskite compound and polymeric hole conductors. *Nat Photonics* **7**, 486–491 (2013).
3. Ponseca, C. S. *et al.* Organometal halide perovskite solar cell materials rationalized: Ultrafast charge generation, high and microsecond-long balanced mobilities, and slow recombination. *J Am Chem Soc* **136**, 5189–5192 (2014).
4. Aydin, E. *et al.* Enhanced optoelectronic coupling for perovskite/silicon tandem solar cells. *Nature* **623**, 732–738 (2023).
5. Park, J. *et al.* Controlled growth of perovskite layers with volatile alkylammonium chlorides. *Nature* **616**, 724–730 (2023).
6. Lin, R. *et al.* All-perovskite tandem solar cells with 3D/3D bilayer perovskite heterojunction. *Nature* **620**, 994–1000 (2023).
7. Liu, C. *et al.* Bimolecularly passivated interface enables efficient and stable inverted perovskite solar cells. *Science (1979)* **382**, 810–815 (2023).
8. Tian, W., Zhou, H. & Li, L. Hybrid Organic–Inorganic Perovskite Photodetectors. *Small* **13**, (2017).
9. Pintor Monroy, M. I. *et al.* All-Evaporated, All-Inorganic $CsPbI_3$ Perovskite-Based Devices for Broad-Band Photodetector and Solar Cell Applications. *ACS Appl Electron Mater* **3**, 3023–3033 (2021).
10. Elkhouly, K. *et al.* Electrically assisted amplified spontaneous emission in perovskite light-emitting diodes. *Nat Photonics* **18**, 132–138 (2024).
11. Wei, Y., Cheng, Z. & Lin, J. An overview on enhancing the stability of lead halide perovskite quantum dots and their applications in phosphor-converted LEDs. *Chem. Soc. Rev* **48**, 310 (2019).
12. Zhu, H. *et al.* Lead halide perovskite nanowire lasers with low lasing thresholds and high quality factors. *Nat Mater* **14**, 636–642 (2015).
13. Zhang, X., Turiansky, M. E. & Van de Walle, C. G. All-inorganic halide perovskites as candidates for efficient solar cells. *Cell Rep Phys Sci* **2**, (2021).
14. Handa, T., Tahara, H., Aharen, T. & Kanemitsu, Y. Large negative thermo-optic coefficients of a lead halide perovskite. *Sci Adv* **5**, (2019).
15. Dong, Z. *et al.* High-Temperature Perovskite Solar Cells. *Solar RRL* **5**, 2100370 (2021).
16. Li, G. *et al.* Structure and Performance Evolution of Perovskite Solar Cells under Extreme Temperatures. *Adv Energy Mater* **12**, (2022).
17. Steele, J. A. *et al.* An embedded interfacial network stabilizes inorganic $CsPbI_3$ perovskite thin films. *Nature Communications 2022 13:1* **13**, 1–11 (2022).
18. Steele, J. A. *et al.* Thermal unequilibrium of strained black $CsPbI_3$ thin films. *Science (1979)* **365**, 679–684 (2019).
19. Mariotti, S. *et al.* Stability and Performance of CsPbI2Br Thin Films and Solar Cell Devices. *ACS Appl Mater Interfaces* **10**, 3750–3760 (2018).
20. Kosasih, F. U., Erdenebileg, E., Mathews, N., Mhaisalkar, S. G. & Bruno, A. Thermal evaporation and hybrid deposition of perovskite solar cells and mini-modules. *Joule* vol. 6 2692–2734 Preprint at https://doi.org/10.1016/j.joule.2022.11.004 (2022).

21. Tong, G. *et al.* High Efficient Hole Extraction and Stable All-Bromide Inorganic Perovskite Solar Cells via Derivative-Phase Gradient Bandgap Architecture. *Solar RRL* **3**, 1900030 (2019).
22. Yan, J. *et al.* Vacuum Deposited Perovskites with a Controllable Crystal Orientation. *Journal of Physical Chemistry Letters* **14**, 8787–8795 (2023).
23. Yan, J. *et al.* Crystallization Process for High-Quality $Cs_{0.15}FA_{0.85}PbI_{2.85}Br_{0.15}$ Film Deposited via Simplified Sequential Vacuum Evaporation. *ACS Appl Energy Mater* **6**, 10265–10273 (2023).
24. Liu, S., Biju, V. P., Qi, Y., Chen, W. & Liu, Z. Recent progress in the development of high-efficiency inverted perovskite solar cells. *NPG Asia Materials* vol. 15 Preprint at https://doi.org/10.1038/s41427-023-00474-z (2023).
25. Zhang, Z. *et al.* Efficient Thermally Evaporated γ-CsPbI3 Perovskite Solar Cells. *Adv Energy Mater* **11**, (2021).
26. Dong, C. *et al.* Growth Mechanism of Thermally Evaporated γ-$CsPbI_3$ Film. *Adv Funct Mater* **33**, 2214414 (2023).
27. Steele, J. A. *et al.* How to GIWAXS: Grazing Incidence Wide Angle X-Ray Scattering Applied to Metal Halide Perovskite Thin Films. *Adv Energy Mater* (2023) doi:10.1002/AENM.202300760.
28. Fujiwara, H. & Collins, R. W. *Spectroscopic Ellipsometry for Photovoltaics Volume 1: Fundamental Principles and Solar Cell Characterization*. vol. 212 (2018).
29. Jiang, Y. *et al.* Temperature dependent optical properties of $CH_3NH_3PbI_3$ perovskite by spectroscopic ellipsometry. *Appl. Phys. Lett* **108**, 61905 (2016).
30. Yuan, L., Yuan, M., Xu, H., Hou, C. & Meng, X. Moisture-stimulated reversible thermochromic $CsPbI_{3-x}Br_x$ films: In-situ spectroscopic-resolved structure and optical properties. (2021) doi:10.1016/j.apsusc.2021.151484.
31. Yuan, M. *et al.* In Situ Spectroscopic Ellipsometry for Thermochromic $CsPbI_3$ Phase Evolution Portfolio. *J. Phys. Chem. C* **124**, 8014 (2020).
32. Wang, X. *et al.* In Situ Monitoring of Thermal Degradation of $CH_3NH_3PbI_3$ Films by Spectroscopic Ellipsometry. *Journal of Physical Chemistry C* **123**, 1362–1369 (2019).
33. Ma, Q. *et al.* The Effect of Stoichiometry on the Stability of Inorganic Cesium Lead Mixed-Halide Perovskites Solar Cells. (2017) doi:10.1021/acs.jpcc.7b06268.
34. Becker, P. *et al.* Low Temperature Synthesis of Stable γ-CsPbI3 Perovskite Layers for Solar Cells Obtained by High Throughput Experimentation. *Adv Energy Mater* **9**, 1900555 (2019).
35. Bai, F. *et al.* A 0D/3D Heterostructured All-Inorganic Halide Perovskite Solar Cell with High Performance and Enhanced Phase Stability. *Advanced Materials* **31**, 1904735 (2019).
36. Frolova, L. A. *et al.* Highly efficient all-inorganic planar heterojunction perovskite solar cells produced by thermal coevaporation of CsI and PbI_2. *Journal of Physical Chemistry Letters* **8**, 67–72 (2017).
37. Zhang, Z. *et al.* Semitransparent Perovskite Solar Cells with an Evaporated Ultra-Thin Perovskite Absorber. *Adv Funct Mater* (2023) doi:10.1002/adfm.202307471.
38. Lai, P.-T. *et al.* All-Vacuum-Deposited Perovskite X-ray Detector with a Record-High Self-Powered Sensitivity of 1.2 C Gy −1 cm −3. *ACS Appl. Mater. Interfaces* (2022) doi:10.1021/acsami.2c03114.
39. Schötz, K. *et al.* Double peak emission in lead halide perovskites by self-absorption. *J Mater Chem C Mater* **8**, 2289–2300 (2020).

40. Aspnes, D. E., Theeten', J. B. & Hottier, F. Investigation of effective-medium models of microscopic surface roughness by spectroscopic ellipsometry. *Phys Rev B* **20**, 3292–3302 (1979).
41. Zhao, M., Shi, Y., Dai, J. & Lian, J. Ellipsometric study of the complex optical constants of a $CsPbBr_3$ perovskite thin film. *J. Mater. Chem. C* **6**, 10450 (2018).
42. Marronnier, A. *et al.* Electrical and optical degradation study of methylammonium-based perovskite materials under ambient conditions. (2018) doi:10.1016/j.solmat.2018.01.020.
43. Akagawa, M. & Fujiwara, H. High-precision characterization of textured a-Si:H/SnO_2:F structures by spectroscopic ellipsometry. *J. Appl. Phys* **110**, 73518 (2011).
44. Fujiwara, H. *et al.* Determination and interpretation of the optical constants for solar cell materials. *Appl Surf Sci* **421**, 276–282 (2017).
45. Marronnier, A. *et al.* Anharmonicity and Disorder in the Black Phases of Cesium Lead Iodide Used for Stable Inorganic Perovskite Solar Cells. *ACS Nano* **12**, 3477–3486 (2018).
46. Wu, S.-C. *et al.* Carrier–Phonon Interaction Induced Large Negative Thermal-Optic Coefficient at Near Band Edge of Quasi-2D $(PEA)_2PbBr_4$ Perovskite. *Adv Funct Mater* **33**, 2213427 (2023).
47. Fujigaki, T., Takagi, S. & Takenaka, M. High-efficiency Ge thermo-optic phase shifter on Ge-on-insulator platform. *Opt Express* **27**, (2019).
48. Komma, J., Schwarz, ; C, Hofmann, ; G, Heinert, ; D & Nawrodt, ; R. Thermo-optic coefficient of silicon at 1550 nm and cryogenic temperatures. *Appl. Phys. Lett* **101**, 41905 (2012).
49. Rao, S. *et al.* Temperature dependence of the thermo-optic coefficient in 4H-SiC and GaN slabs at the wavelength of 1550 nm. *Sci Rep* **12**, (2022).
50. Handa, T. *et al.* Large thermal expansion leads to negative thermo-optic coefficient of halide perovskite $CH_4NH_3PbCl_3$. *Phys Rev Mater* **4**, (2020).
51. Zhang, C. *et al.* Unraveling Urbach Tail Effects in High-Performance Organic Photovoltaics: Dynamic vs Static Disorder. *ACS Energy Lett* **7**, 1971–1979 (2022).
52. Urbach, F. The Long-Wavelength Edge of Photographic Sensitivity of the Electronic Absorption of Solids. *Physical Review* **92**, 1324–1324 (1953).
53. Rajagopal, A., Liang, P. W., Chueh, C. C., Yang, Z. & Jen, A. K. Y. Defect Passivation via a Graded Fullerene Heterojunction in Low-Bandgap Pb-Sn Binary Perovskite Photovoltaics. *ACS Energy Lett* **2**, 2531–2539 (2017).
54. Ledinsky, M. *et al.* Temperature Dependence of the Urbach Energy in Lead Iodide Perovskites. *Journal of Physical Chemistry Letters* **10**, 1368–1373 (2019).
55. Singh, S. *et al.* Effect of Thermal and Structural Disorder on the Electronic Structure of Hybrid Perovskite Semiconductor $CH_3NH_3PbI_3$. *Journal of Physical Chemistry Letters* **7**, 3014–3021 (2016).
56. De Wolf, S. *et al.* Organometallic halide perovskites: Sharp optical absorption edge and its relation to photovoltaic performance. *Journal of Physical Chemistry Letters* **5**, 1035–1039 (2014).
57. Falsini, N. *et al.* Analysis of the Urbach tail in cesium halide perovskites. *J. Appl. Phys* **131**, 10902 (2022).
58. Kurik, M. V. Urbach rule. *physica status solidi (a)* **8**, 9–45 (1971).
59. Kim, G. *et al.* Impact of strain relaxation on performance of α-formamidinium lead iodide perovskite solar cells. *Science (1979)* **370**, 108–112 (2020).

60. Mannino, G. *et al.* Temperature-Dependent Optical Band Gap in $CsPbBr_3$, $MAPbBr_3$, and $FAPbBr_3$ Single Crystals. *Journal of Physical Chemistry Letters* **11**, 2490–2496 (2020).
61. Ceratti, D. *et al.* $CsPbBr_3$, $MAPbBr_3$, and $FAPbBr_3$ bromide perovskite single crystals: Interband critical points under dry n2 and optical degradation under humid air. *Journal of Physical Chemistry C* **125**, 4938–4945 (2021).
62. Chen, Y. *et al.* The distinctive phase stability and defect physics in $CsPbI_2Br$ perovskite. (2019) doi:10.1039/c9ta04839a.
63. Parida, B. *et al.* Two-step growth of $CsPbI_{3-x}Br_x$ films employing dynamic CsBr treatment: toward all-inorganic perovskite photovoltaics with enhanced stability. (2019) doi:10.1039/c9ta05948b.
64. Igual-Muñoz, A. M. *et al.* Room-Temperature Vacuum Deposition of $CsPbI_2Br$ Perovskite Films from Multiple Sources and Mixed Halide Precursors. *Chemistry of Materials* **32**, 8641–8652 (2020).
65. Mali, S. S. *et al.* Implementing Dopant-Free Hole-Transporting Layers and Metal-Incorporated $CsPbI_2Br$ for Stable All-Inorganic Perovskite Solar Cells. *ACS Energy Lett* **6**, 778–788 (2021).
66. Handa, T., Yamada, T., Nagai, M. & Kanemitsu, Y. Phonon, thermal, and thermo-optical properties of halide perovskites. *Phys. Chem. Chem. Phys* **22**, 26069–26087 (2020).
67. Foley, B. J. *et al.* Temperature dependent energy levels of methylammonium lead iodide perovskite. *Appl. Phys. Lett* **106**, 243904 (2015).
68. Ashiotis, G. *et al.* The fast azimuthal integration Python library: PyFAI. *J Appl Crystallogr* **48**, 510–519 (2015).
69. Rodriguez-Carvajal, J. Recent advances in magnetic structure determination neutron powder diffraction. *Physica B* **192**, 113 (1993).
70. Burkhard, G. F., Hoke, E. T. & McGehee, M. D. Accounting for interference, scattering, and electrode absorption to make accurate internal quantum efficiency measurements in organic and other thin solar cells. *Advanced Materials* **22**, 3293–3297 (2010).